Editors' Suggestion

Probing Hydrodynamic Fluctuation-Induced Forces with an Oscillating Robot

Steven W. Tarr,[1] Joseph S. Brunner,[1,2] Daniel Soto,[1] and Daniel I. Goldman[1,*]
[1] *School of Physics, Georgia Institute of Technology, 837 State Street, Atlanta, Georgia 30332, USA*
[2] *Department of Radiation Medicine, University of Kentucky, 800 Rose Street, Lexington, Kentucky 40536, USA*

(Received 8 May 2023; revised 14 August 2023; accepted 16 January 2024; published 20 February 2024)

We study the dynamics of an oscillating, free-floating robot that generates radially expanding gravity-capillary waves at a fluid surface. In open water, the device does not self-propel; near a rigid boundary, it can be attracted or repelled. Visualization of the wave field dynamics reveals that when near a boundary, a complex interference of generated and reflected waves induces a wave amplitude fluctuation asymmetry. Attraction increases as wave frequency increases or robot-boundary separation decreases. Theory on confined gravity-capillary wave radiation dynamics developed by Hocking in the 1980s captures the observed parameter dependence due to these "Hocking fields." The flexibility of the robophysical system allows detailed characterization and analysis of locally generated nonequilibrium fluctuation-induced forces [M. Kardar and R. Golestanian, Rev. Mod. Phys. **71**, 1233 (1999)].

DOI: 10.1103/PhysRevLett.132.084001

Forces mediated by steady-state fluctuations in fields are well studied in diverse systems [1–5]. In confinement, emergent wave field asymmetries can produce nonzero, net fluctuation-induced forces on boundaries; such forces are observed across scales, from the quantum mechanical vacuum [1–3,6,7] to fluids [4,5,8–12]. In quantum mechanics, the Casimir effect demonstrates that nearby neutral plates confine and modify zero-point-energy wave fields, often yielding attraction [1–3,6,7]. In driven fluid systems, boundaries generate an analogous downsampling of surface wave modes called the "maritime Casimir effect" [5,8]. The downsampled modes reduce the radiation pressure between objects at the fluid surface and can be observed as reduced amplitude waves [5,8,9,13].

More recently, researchers studying nonequilibrium fluctuation-induced forces have uncovered a variety of Casimir-like phenomena that demonstrate long-range attraction and repulsion in diverse systems including complex fluids, fluid membranes, and vibrofluidized granular media [13–19]. Such systems sustain additional effects owed to their nonequilibrium dynamics including generic power law correlations [19], violations of Newton's third law [15], and migration toward colder regions [14]. Indeed, the past 30 years have generated expansive literature on Casimir and Casimir-like forces. However, to our knowledge, these forces have not been leveraged for self-propulsion. The capacity for locomotion stemming from symmetric momentum generation is novel and stands in contrast to typical asymmetric inertial self-propulsion (e.g., body bending [20–24], wave expulsion [25–28], spinning propellers [29]).

Here we introduce a system that allows not only for convenient creation and visualization of non-equilibrium fluctuation-induced forces using surface waves but also for probing a new regime where the agents subject to fluctuation-induced forces are themselves producing the requisite fluctuations. In doing so, we also discover that self-propulsion can be induced in a free-floating, oscillating robophysical system that does not directly generate asymmetric momentum transport. Symmetrically propagating waves undergo a complex interference when reflected at a boundary, breaking symmetry and generating propulsive radiation forces. We probe the dynamics with a custom-developed robot and map radiation forces as both oscillation frequency and confinement distance vary. Confinement on one side leads to a modification in wave field amplitude, and the dependence of the consequent radiation force on oscillation frequency can be quantitatively explained by theory for gravity-capillary waves developed by Hocking [30–32]. Further, we demonstrate the capacity for fluctuation-induced forces in systems with monochromatic fluctuations as opposed to the typical noisy spectra [1–6,9,13,17,19,33]. Given the importance of the seldom-studied generation and reflection properties of gravity-capillary waves to the boat's locomotion, we refer to these confined, asymmetric wave fields as "Hocking fields."

Apparatus and fundamental behaviors.—The robotic boat (total mass $m = 368$ g) consists of a circularly symmetric hull of radius $R_B = 6$ cm, a custom circuit board, two fan motors (uxcell Coreless Micro Motor 412), and an eccentric motor (Vybronics Inc. Cylindrical Vibration Motor VJQ24-35K270B). The boat's hull was 3D printed in Polymaker PolyLite™ PLA and waterproofed with marine epoxy. All electronics and batteries were mounted onboard, and additional weights were added such that a free-floating boat at rest is level to within 1°. We mounted the eccentric motor beneath the electronics; when enabled, the motor vibrates the boat with power-dependent frequency ω primarily along the fore-aft axis (roll) with minimal vertical

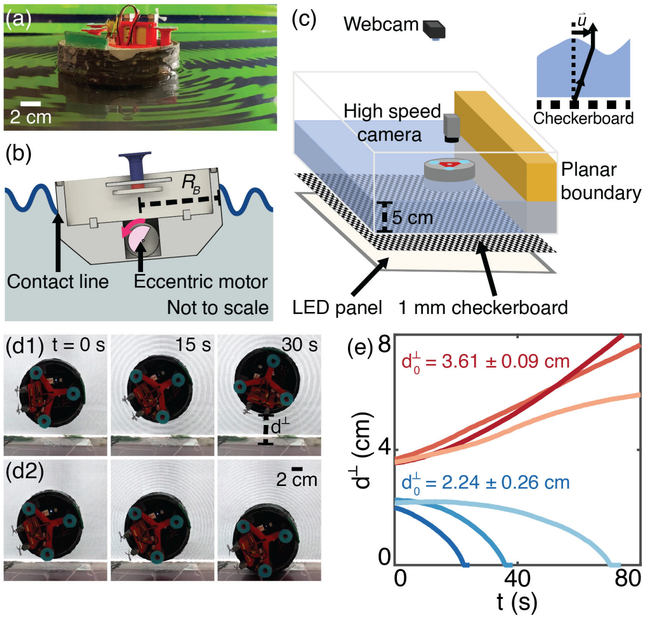

FIG. 1. Wave-generating robot boat. (a) Photo of boat generating 17.1 Hz waves. (b) Schematic of the eccentric motor vibrating the boat to generate waves; propellers shown in (a) are not used in this study and thus omitted in (b). (c) Diagram of the tank wherein all experiments were performed. A backlit checkerboard enables Fast Checkerboard Demodulation for spatiotemporal surface reconstruction [41]. (Inset) Fast Checkerboard Demodulation determines fluid surface height using the instantaneous distortion of a checkerboard by surface perturbations. (d1)–(d2) Time series of repulsion from (17.1 Hz) and attraction toward (33.5 Hz) wall, respectively. (e) Evolution of perpendicular hull-wall distance for repeated repulsive and attractive trials at 17.1 Hz and two different initial distances.

motion or induced surface currents. Beyond $\omega = 20$ Hz, the vibration tends toward roll amplitude $0.15° \pm 0.02°$, pitch (left-right axis) amplitude $0.05° \pm 0.01°$, and vertical oscillation amplitude 0.09 ± 0.02 mm (see Supplemental Material [34]). The result is a left-right and fore-aft symmetric, radially emanated, monochromatic wave train of wavelength $\lambda(\omega)$ traveling along the fluid surface [Figs. 1(a) and 1(b), Movie S1 in the Supplemental Material [34]].

Because of the symmetries of the emitted waves, a boat placed far from boundaries experiences no net radiation force F_W. Upon breaking symmetry by approaching a boundary, F_W becomes nonzero, and the boat self-propels [Figs. 1(d1) and 1(d2), Movie S2 [34]]. We observe both repulsive and attractive behaviors [Fig. 1(e)], with repulsion occurring more weakly such that it is often indistinguishable from noise.

To probe these dynamics, we placed the boat near a rigid acrylic planar boundary extending from the floor above the water (61 cm long, 30 cm tall, vertical to within 1°), varied both ω and initial hull-boundary distance $d_0^\perp$, and allowed the boat to move freely in response to F_W. Though we were unable to prescribe wave amplitude A independently from

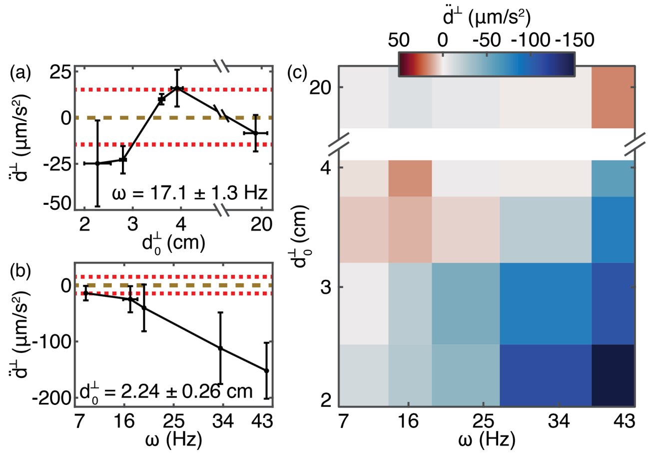

FIG. 2. Wave-generating boat experiences attraction and repulsion near boundaries. (a)–(b) $\ddot{d}^\perp$ versus $d_0^\perp$ and ω. Red dotted lines denote the system's noise interval determined by behavior far from boundaries. Simultaneous dependence on both parameters is shown in (c), where each box corresponds to the average of 5 trials.

ω, we expect it to affect F_W in accord with established theory on the energy of surface waves [42,43]. We chose a wall with length $\ell \gg R_B, \lambda$ such that we may treat our system as quasi-1D and study the boat's motion along the axis normal to the wall. Any observed parallel motion had no clear bias. For all experiments, we programmed a motor controller to ramp the eccentric motor up linearly to the target frequency over 10 s to minimize transients.

We recorded images of trials with a Logitech C920 webcam at 30 FPS and tracked the boat's lateral motion with color-thresholding code in MATLAB. We extracted the boat's perpendicular acceleration $\ddot{d}^\perp$ by fitting a quadratic equation to the position-time data prior to any drag-induced inflection point. We observed an increasingly attractive force with decreasing $d_0^\perp$ and increasing ω [Figs. 2(a) and 2(b)]. During some trials with high $d_0^\perp$ and low ω, a lightly repulsive F_W emerged. For particularly high $d_0^\perp$, the boat was considered to be "far from boundaries"; the wave field symmetry was restored and the boat experienced a near-zero F_W. We refer to the threshold distance separating the attractive and repulsive regimes as $d_T^\perp(\omega)$ (see Supplemental Material [34]).

Direct measurement of wave force.—Having observed $\mathcal{O}(\ddot{d}^\perp) \leq 10^2$ μm/s² across all tested initial conditions, we sought to isolate F_W from any transient effects (e.g., viscous [44] and wave [23,45] drag, inertia [46]) that could dampen the system's evolution and result in such a minuscule acceleration. We investigated F_W alone by restricting the boat's motion to that of a simple pendulum without impeding vibration [Fig. 3(a)], a method similarly employed to quantify water wave analog Casimir forces [9]. The boat was affixed along its central axis 1.3 cm above the water line to a thin fishing line of length $L = 1.4$ m via

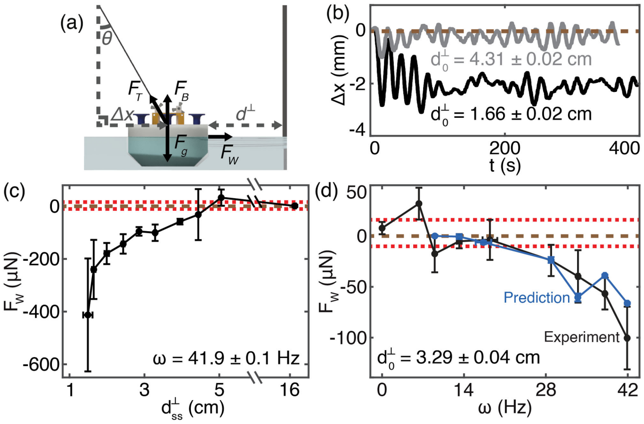

FIG. 3. Measurement of near-boundary propulsive force and its parameter dependence. (a) Diagram for pendulum experiments used to directly measure F_W. (b) Archetypal boat displacement plots for pendulum experiments at 33.5 Hz and two different initial distances. Oscillations are attributed to the interplay between F_W and F_T. (c)–(d) F_W versus $d_{\text{ss}}^{\perp}$ and ω. Red dotted lines denote the system's noise interval determined by behavior far from boundaries. Blue line in (d) indicates theoretical prediction using measurements in Fig. 4 and Eq. (3).

a bowline knot. We calibrated the line such that when the pendulum angle θ was zero, the tension force F_T too was zero. For nonzero F_W, the boat's resultant displacement Δx caused F_T to increase until reaching force balance [Fig. 3(b)]. We measured Δx for a variety of ω (0–42 Hz) and $d_0^{\perp}$ (1.9–3.8 cm) and observed typical values within 0–3 mm. Since $L \gg \Delta x$, we assume the boat undergoes negligible vertical displacement [47].

By measuring Δx in steady state, we can estimate the perpendicular wave force $\vec{F}_W = (m - \rho V) g \Delta \vec{x} / L$, where ρ is the fluid density and V is the liquid volume displaced by the boat. We plotted F_W as a function of the steady-state hull-wall distance $d_{\text{ss}}^{\perp}$ and ω [Figs. 3(c) and 3(d)]. We include a heat map of all force data in Fig. S4 [34]. As expected, the qualitative behavior of F_W closely resembles that of the acceleration, with increasing attraction below, light repulsion near, and near-zero effects above $d_T^{\perp}(\omega)$. Despite the removal of transient effects, attractive and repulsive forces remained small, respectively demonstrating $\mathcal{O}(F_W) \in [10^1, 10^2]$ and $[10^0, 10^1]$ μN. We note that most measurements with $d_{\text{ss}}^{\perp} < d_T^{\perp}$ fall outside the experimental noise interval 2.9 ± 13.1 μN.

Surface wave measurements.—To better understand the role of the emanated waves in generating a locomotive force, we employed the synthetic [48] Schlieren visualization technique Fast Checkerboard Demodulation [41] (see Supplemental Material [34]) to obtain quantitative measurements of the wave field [Figs. 1(c), 4(a), and 4(b), Movie S3 [34]). For optimal visualization quality, we minimized the water's depth to $h_{\text{rest}} = 5$ cm for all experiments. Imaging was performed with a high speed camera (AOS X-PRI) at 500 FPS when the system had reached steady state and processed using custom MATLAB code derived from Refs. [41,50]. We observed the wave train to follow $A \propto r^{-1/2}$ in accord with established surface wave theory and follow the known dispersion relation for gravity-capillary waves:

$$\omega^2(k) = \left(gk + \frac{\gamma k^3}{\rho}\right) \tanh\left(h_{\text{rest}} k\right), \qquad (1)$$

where γ is the fluid's surface tension, k is the wave number, and g is the standard gravity (see Supplemental Material [34]) [42].

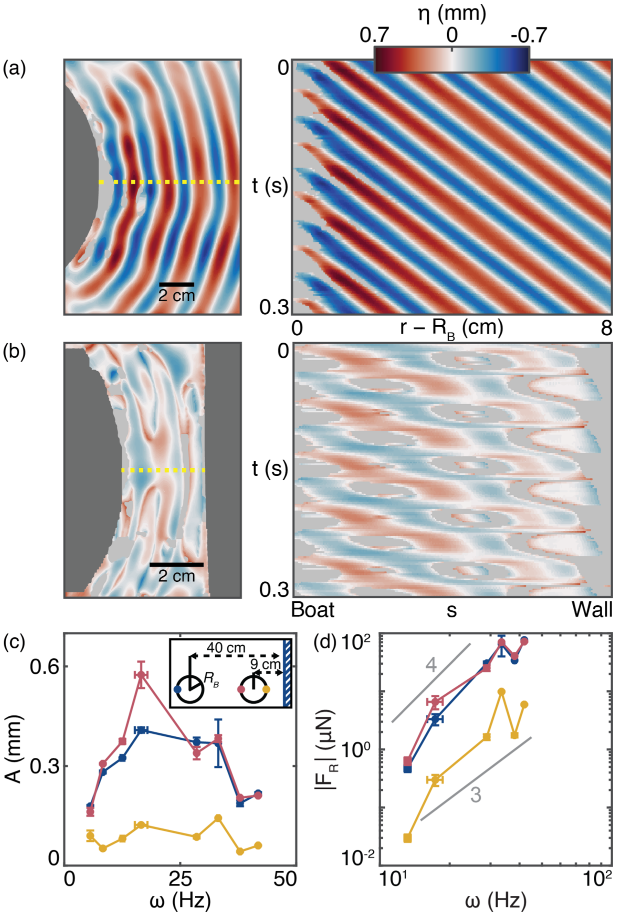

FIG. 4. Visualization and quantification of near-robot gravity-capillary wave fields. (a)–(b) Reconstructions of 17.1 Hz waves far from and near a boundary, respectively, with space-time heat maps corresponding to dotted yellow lines. $\eta(t, \vec{r})$ describes the free surface height with respect to h_{rest}. Dark gray regions were occupied by solid objects (e.g., boat, wall). Light gray regions were deemed unreconstructable (see Supplemental Material [34]). (c) Fast Checkerboard Demodulation measurements reveal the net field near the wall to have reduced $A(\omega)$. (d) Radiation forces on boat sides due to emitted gravity-capillary waves as predicted by Eq. (3) and panel (c). Solid gray lines denote scaling of ω^3 and ω^4.

Fast Checkerboard Demodulation analysis of steady-state waves between the boat and wall reveals a net field propagating outward from the boat [Fig. 4(b)]. These waves share ω with those emitted on the boat's far side and far from boundaries, but possess reduced A regardless of ω [Fig. 4(c)]. We surmise that when the boat is sufficiently close to the wall, reflected waves return with non-negligible energy and modulate the free surface height at the hull. This modulation impedes concurrent wave generation on the side nearest the wall while minimally affecting the opposite side. Consequently, the steady-state amplitude between the hull and wall is reduced. We liken these dynamics to the reductions in height when jumping off a deformable medium [51] or pumping a swing with poor timing [52].

A hydrodynamic model.—Armed with an understanding of the wave fields both near and far from boundaries, we motivate the boat's locomotive behavior as it relates to $d^{\perp}$ [Fig. 5]. The existence of a radiative force incident on a wave emitter and proportional to square amplitude is a classical result [42,43] observed in many systems with asymmetric wave generation [5,9,27]. When the boat is far from boundaries, the generated waves are spatially symmetric, leading to a net-zero F_W. Near boundaries, reflected waves induce an amplitude asymmetry, resulting in a finite F_W. We postulate that at a certain $d_T^{\perp}$, the reflected wave will have insufficient energy to generate the asymmetric Hocking field. However, the reflected wave will not have dissipated enough for the boat to be considered far from boundaries; instead, the impingement of the reflected wave on the boat will lightly force it away from the wall.

Though the amplitude dynamics successfully describe the boat's attraction and motionlessness for small and large $d^{\perp}$ respectively, they provide insufficient reasoning for F_W's observed frequency dependence. As indicated in Refs. [1,4,19], such nonequilibrium amplitude dynamics will necessarily depend on specific details of the system. Therefore, we hypothesize that the unique properties of gravity-capillary waves are relevant to these complex hydrodynamics. Work by Hocking on the interactions of gravity-capillary waves with hard surfaces emphasizes the importance of wave number (alternatively frequency) to radiation and reflection [30–32]. Upon reflecting off a rigid boundary, gravity-capillary waves dissipate substantial energy through complex contact-line dynamics [53]. Within the accessible wave number range for our boat, the reflection coefficient $R < 0.22$ with $R \propto k^3$ and $k^{0.85}$ for $k \lesssim 7\ \mathrm{m}^{-1}$ and $k \gtrsim 20\ \mathrm{m}^{-1}$ respectively [30]. Coupled with the aforementioned amplitude modulation, this wave number dependence suggests that higher frequency waves will have sufficient energy to induce attraction at farther hull-wall distances.

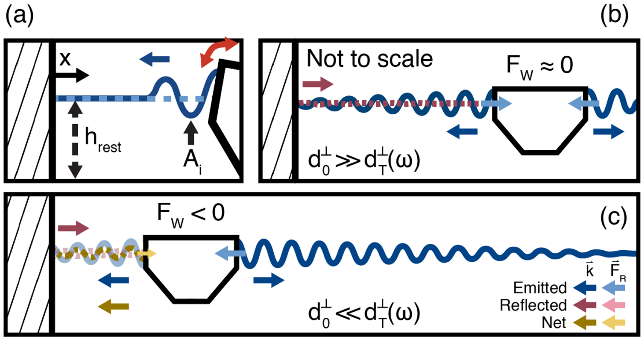

FIG. 5. Hypothesis for attractive self-propulsion via Hocking field generation. (a) Regardless of $d_0^{\perp}$, the boat initially generates a symmetric wave field. (b) When $d_0^{\perp} \gg d_T^{\perp}$, the reflected waves have insufficient energy to affect the boat. (c) When $d_0^{\perp} \ll d_T^{\perp}$, the reflected waves perturb the free-surface height at the boat, yielding a reduced-amplitude field. This amplitude asymmetry produces a net radiation force toward the boundary measured and predicted in Fig. 3.

Further, gravity-capillary waves radiated by a vertically oscillating body have energy given by the following [32]:

$$E_R = \frac{\pi}{2}\left(1 + \frac{3\gamma k^2}{\rho g}\right)A^2. \tag{2}$$

Considering the boat as two back-to-back, semicircular wave emitters, this expression implies the following radiation force incident upon one side:

$$|F_R(k)| = \frac{E_R k}{4\pi} = \left(\frac{k}{8} + \frac{3\gamma k^3}{8\rho g}\right)A^2\left(\omega(k)\right). \tag{3}$$

The factor of 4π accounts for projecting the wave momentum normal to the semicircular boundary (see, e.g., Ref. [5] for a more detailed derivation). For our boat which has nontrivial $A(\omega)$ [Fig. 4(c)], the predicted $F_R(\omega)$ follows a power law with exponent between 3 and 4 [Fig. 4(d)]. We reiterate that the amplitude measurements were taken within the attractive regime, and so we shift the origin of our power law to the observed threshold frequency for attraction. The difference between F_R on either side of the boat yields a predicted F_W; this prediction matches well with experimental results without any fitting parameters [Fig. 3(d)].

We summarize our postulated model of the boat's boundary-driven locomotion in four regimes. In all cases, when the boat first emits waves, the field is symmetric, leading to a net-zero radiation force on the boat [Fig. 5(a)]. When $d_0^{\perp} \gg d_T^{\perp}$, the waves reflected off the boundary return to the boat with negligible energy compared to emission. Consequently, the boat experiences a force negligibly close to zero [Fig. 5(b)]. When $d_0^{\perp} \ll d_T^{\perp}$, the reflected waves hinder wave generation between the boat and wall, leading to an observed amplitude reduction. Meanwhile, waves on the far side remain unchanged; this broken symmetry yields a net force appearing as a boat-wall attraction [Fig. 5(c)]. When approaching $d_T^{\perp}$ from $d_0^{\perp} > d_T^{\perp}$, reflected waves have insufficient amplitude to affect wave generation but still carry non-negligible momentum. Symmetry is again broken and the boat experiences a slight repulsive force. Since the energy of a reflected gravity-capillary wave increases with k, $d_T^\perp$ also increases with k (and, consequently, ω). Should the original choice of $d_0^\perp$ be retained while increasing ω, the reflected waves will then have sufficient energy to affect wave generation, causing the same result as when $d_0^\perp \ll d_T^\perp$.

We note that our model can only explain the boat's steady-state position using wave amplitudes measured in that state. In 1D simulations of a free-floating boat that responds to the measured steady-state wave force and drag, the simulated boat always reaches the boundary faster than in experiment (see Supplemental Material [34]). An interesting notion is that the moving boat may experience a weaker wave force than in steady state due to the wave field's finite propagation time. In a dynamical system, the ever-changing boundary conditions may limit the extent to which the wave field can respond and evolve, leading to weaker transient fluctuation-induced forces. Additionally, Hocking's theories on gravity-capillary waves require both the emitter and reflecting boundary to be stationary on average. A much harder problem then is computing the system dynamics as the wave field updates; how would one compute the position versus time of the attracting boat in a dynamic environment? Indeed, we find the boat exhibits complex attractive modes like "towing" in response to a moving boundary (see Supplemental Material [34], Movie S5). These dynamical experiments will help characterize transient locomotive states owed to Hocking fields in stationary and active environments.

Conclusion.—In this Letter, we revealed how a symmetrically oscillating robot can use confined hydrodynamic surface wave fields—which we refer to as Hocking fields—to locomote without the need for a traditional propulsion mechanism and made the first direct measurement of the corresponding force. In doing so, we add to the growing list of fluctuation-induced forces that employ surface wave fields both for propulsion and nonlocal interaction with fellow substrate occupants [5,8–13,15–19,25–28,54–57]. By symmetrically generating waves near a boundary, our boat takes advantage of the reflection dynamics unique to gravity-capillary waves to self-propel exclusively via wave drag with frequency- and distance-dependent locomotive modes. Our robophysical approach enables a convenient method to discover features of nonequilibrium, self-induced fluctuation-induced forces. The flexibility of this approach encourages future experiments that are not strictly limited to the fluid surface. Practically, manipulation of oscillation spectrum in response to transient conditions may prove valuable in expanding the range and strength of such interactions.

We thank Enes Aydin for designing and constructing the tank apparatus and for helping during the boat design phase. We thank Ryan Hirsh for assisting with pendulum experiments. We thank Paul Umbanhowar for helpful comments and discussion. This work was funded by the Army Research Office Grants No. GR00008673, No. W911NF2110033 and a Dunn Family Professorship (D. I. G.).

---

[*] Corresponding author: daniel.goldman@physics.gatech.edu

[1] M. Kardar and R. Golestanian, Rev. Mod. Phys. **71**, 1233 (1999).

[2] H. B. G. Casimir and D. Polder, Phys. Rev. **73**, 360 (1948).

[3] H. B. G. Casimir, Proc. K. Ned. Akad. Wet. **51**, 793 (1948).

[4] H. Li and M. Kardar, Phys. Rev. Lett. **67**, 3275 (1991).

[5] A. A. Lee, D. Vella, and J. S. Wettlaufer, Proc. Natl. Acad. Sci. U.S.A. **114**, 9255 (2017).

[6] G. L. Klimchitskaya, U. Mohideen, and V. M. Mostepanenko, Rev. Mod. Phys. **81**, 1827 (2009).

[7] L. M. Woods, D. A. R. Dalvit, A. Tkatchenko, P. Rodriguez-Lopez, A. W. Rodriguez, and R. Podgornik, Rev. Mod. Phys. **88**, 045003 (2016).

[8] S. L. Boersma, Am. J. Phys. **64**, 539 (1996).

[9] B. C. Denardo, J. J. Puda, and A. Larraza, Am. J. Phys. **77**, 1095 (2009).

[10] D. M. Harris, J. Moukhtar, E. Fort, Y. Couder, and J. W. M. Bush, Phys. Rev. E **88**, 011001(R) (2013).

[11] G. Pucci, P. J. Sáenz, L. M. Faria, and J. W. M. Bush, J. Fluid Mech. **804**, R3 (2016).

[12] P. J. Sáenz, G. Pucci, S. E. Turton, A. Goujon, R. R. Rosales, J. Dunkel, and J. W. M. Bush, Nature (London) **596**, 58 (2021).

[13] C. Parra-Rojas and R. Soto, Phys. Rev. E **90**, 013024 (2014).

[14] A. Najafi and R. Golestanian, Europhys. Lett. **68**, 776 (2004).

[15] P. R. Buenzli and R. Soto, Phys. Rev. E **78**, 020102(R) (2008).

[16] A. Hanke, PLoS One **8**, e53228 (2013).

[17] D. Ray, C. Reichhardt, and C. J. Olson Reichhardt, Phys. Rev. E **90**, 013019 (2014).

[18] R. Ni, M. A. Cohen Stuart, and P. G. Bolhuis, Phys. Rev. Lett. **114**, 018302 (2015).

[19] A. Aminov, Y. Kafri, and M. Kardar, Phys. Rev. Lett. **114**, 230602 (2015).

[20] E. M. Purcell, Am. J. Phys. **45**, 3 (1977).

[21] R. D. Maladen, Y. Ding, C. Li, and D. I. Goldman, Science **325**, 314 (2009).

[22] V. Kantsler, J. Dunkel, M. Polin, and R. E. Goldstein, Proc. Natl. Acad. Sci. U.S.A. **110**, 1187 (2013).

[23] K. Diaz, B. Chong, S. Tarr, E. Erickson, and D. I. Goldman, arXiv:2210.09570.

[24] B. Chong, J. He, S. Li, E. Erickson, K. Diaz, T. Wang, D. Soto, and D. I. Goldman, Proc. Natl. Acad. Sci. U.S.A. **120**, e2213698120 (2023).

[25] C. Roh and M. Gharib, Proc. Natl. Acad. Sci. U.S.A. **116**, 24446 (2019).

[26] K. Y. Lee, L. Wang, J. Qu, and K. R. Oldham, in *International Conference on Manipulation, Automation and Robotics at Small Scales* (IEEE, Helsinki, Finland, 2019), pp. 1–6, 10.1109/MARSS.2019.8860988.

[27] E. Rhee, R. Hunt, S. J. Thomson, and D. M. Harris, Bioinspir. Biomim. **17**, 055001 (2022).

[28] G. P. Benham, O. Devauchelle, S. W. Morris, and J. A. Neufeld, Phys. Rev. Fluids **7**, 074804 (2022).

[29] D. Gerr, *Propeller Handbook* (International Marine Publishing, Camden, ME, 1989).

[30] L. M. Hocking, Wave Motion **9**, 217 (1987).

[31] L. M. Hocking, J. Fluid Mech. **179**, 253 (1987).

[32] L. M. Hocking, J. Fluid Mech. **186**, 337 (1988).

[33] C. Cattuto, R. Brito, U. M. B. Marconi, F. Nori, and R. Soto, Phys. Rev. Lett. **96**, 178001 (2006).

[34] See Supplemental Material at http://link.aps.org/supplemental/10.1103/PhysRevLett.132.084001 for additional system details and probes, which includes Refs. [35–40].

[35] W. J. Palm III, *System Dynamics*, 3rd ed. (McGraw-Hill New York, 2014).

[36] M. Tatsuno, S. Inoue, and J. Okabe, Rep. Res. Inst. Appl. Mech. Kyushu Univ. **17**, 195 (1969).

[37] A. Hulme, J. Fluid Mech. **121**, 443 (1982).

[38] S. Taneda, J. Fluid Mech. **227**, 193 (1991).

[39] W. Thielicke and R. Sonntag, J. Open Res. Software **9**, 12 (2021).

[40] S. F. Hoerner, *Fluid-Dynamic Drag: Practical Information on Aerodynamic Drag and Hydrodynamic Resistance* (Hoerner Fluid Dynamics, Bakersfield, CA, 1965).

[41] S. Wildeman, Exp. Fluids **59**, 97 (2018).

[42] H. Lamb, *Hydrodynamics* (University Press, Cambridge, Great Britain, 1924).

[43] M. S. Longuet-Higgins and R. W. Stewart, Deep-Sea Res. **11**, 529 (1964).

[44] K. D. Danov, R. Dimova, and B. Pouligny, Phys. Fluids **12**, 2711 (2000).

[45] T. Burghelea and V. Steinberg, Phys. Rev. Lett. **86**, 2557 (2001).

[46] C. Scholz, S. Jahanshahi, A. Ldov, and H. Löwen, Nat. Commun. **9**, 5156 (2018).

[47] The pendulum angle θ is related to the boat's horizontal displacement Δx by the length of the fishing line L: $\sin\theta = \Delta x/L$. The boat's vertical displacement then must be $\Delta y = L(1-\cos\theta) = L(1-\sqrt{1-\Delta x^2/L^2})$. Typical values of Δx were no larger than 3 mm and $L = 1.4$ m; therefore, the maximum vertical displacement is 3 μm. Considering the order of the boat's radius $\mathcal{O}(R_B) = 10^{-2}$ m and emitted wave amplitude $\mathcal{O}(A) = 10^{-4}$ m, we assume a vertical displacement on the order $\mathcal{O}(\Delta y) \leq 10^{-6}$ m to be negligible.

[48] Classical Schlieren techniques rely on the precise alignment of two light-filtering masks. The replacement of a physical mask with a digitally-generated (synthetic) mask circumvents this non-trivial task (see Ref. [49]).

[49] B. R. Sutherland, S. B. Dalziel, G. O. Hughes, and P. F. Linden, J. Fluid Mech. **390**, 93 (1999).

[50] F. Moisy, M. Rabaud, and K. Salsac, Exp. Fluids **46**, 1021 (2009).

[51] J. Aguilar and D. I. Goldman, Nat. Phys. **12**, 278 (2016).

[52] S. Bae and Y.-H. Kang, Eur. J. Phys. **27**, 75 (2005).

[53] G. Michel, F. Pétrélis, and S. Fauve, Phys. Rev. Lett. **116**, 174301 (2016).

[54] R. S. Wilcox, Science **206**, 1325 (1979).

[55] I. Ho, G. Pucci, A. U. Oza, and D. M. Harris, arXiv: 2102.11694.

[56] Z.-M. Yuan, M. Chen, L. Jia, C. Ji, and A. Incecik, J. Fluid Mech. **928**, R2 (2021).

[57] H. Ko, M. Hadgu, K. Komilian, and D. L. Hu, Phys. Rev. Fluids **7**, 090501 (2022).